ELSEVIER

Materials Science and Engineering A xxx (2007) xxx–xxx

MATERIALS SCIENCE & ENGINEERING A

www.elsevier.com/locate/msea

On the incorporation of length scales associated with pearlitic and bainitic microstructures into a visco-plastic self-consistent model

D. Canadinc [a,*,1], H. Sehitoglu [a,1], H.J. Maier [b,2], P. Kurath [a,1]

[a] *University of Illinois at Urbana-Champaign, Department of Mechanical Science and Engineering, 1206 W. Green Street, Urbana, IL 61801, United States*

[b] *University of Paderborn, Lehrstuhl f. Werkstoffkunde, D-33095 Paderborn, Germany*

Received 17 July 2007; accepted 22 August 2007

Abstract

A visco-plastic self-consistent model was modified to account for strain hardening in steels with pearlitic and bainitic microstructures. Occurrence of slip and the contribution of secondary phases in body-centered cubic steels to the strengthening were simulated for tension, compression and shear loadings. The initial texture and texture evolution at larger strains for bcc polycrystalline steels with intrinsic barriers to dislocation motion were studied under quasi-static conditions. The crystallographic texture of rails undergoing ~~large-shear~~ strains was closely examined and compared to the simulations. The results clearly demonstrate that the method has the capability to predict texture evolution in deformed rails. The methodology offers opportunities for improved materials characterization of various steel microstructures.

Keywords: Crystal plasticity; Anisotropic material; Constitutive behavior; Mechanical testing; Visco-plastic self-consistent algorithm

1. Background and motivation

Steels undoubtedly constitute the most extensively studied group of metallic materials to date, and consequently, the literature offers a wealth of information on various aspects, including modeling of their mechanical response. Despite the existing wealth of knowledge on the subject matter, steels continue to demand attention as new applications that call for improved performance warrant a deeper understanding of the strengthening mechanisms.

Within the last three decades, many numerical simulations were carried out investigating the finite deformation mechanisms, namely slip and twinning, plastic deformation of steels, and its relationship with texture. Nevertheless, to the authors' best knowledge, a model has not been forwarded to date that accounts for the different phases in pearlitic and bainitic steels by incorporating the length scales of obstacles specific to the corresponding microstructure in a simple crystal plasticity formulation.

With this motivation, the present study was undertaken, in order to shed more light onto the occurrence of glide in body-centered cubic (bcc) steels, especially at ~~large-plastic~~ strains. Specifically, the present study focuses on the development of a modified crystal plasticity model that correctly predicts the deformation response by incorporating the role of fine microstructural features of the two-phase bcc steels. The focus is placed on two classes of rail steels, featuring bainitic and pearlitic microstructures. The J6 bainitic steel[3] is a newly developed high-strength steel [1,2], and possesses a bainitic structure, and a hardness of 44 on the Rockwell C (HRC) scale. Its strength is dictated by fine precipitates. The premium rail material, pearlitic steel, has a hardness of 38 HRC [3] and resists plastic deformation due to the fine pearlite lamellae presenting an obstacle to dislocation motion. The J6 bainitic steel has been tested on track by TTCI (Transportation Technology Center Inc., Pueblo ~~Co~~) under various environmental and loading

Q1 * Corresponding author. Current address: Department of Mechanical Engineering, Koc University, Istanbul, Turkey. Tel.: ~~+1 217 333 1176~~; fax: ~~+1 217 244 6534~~.
E-mail addresses: demircan.canadinc@gmail.com, dcanadinc@ku.edu.tr (D. Canadinc).
[1] Tel.: +1 217 333 1176; fax: +1 217 244 6534.
[2] Tel.: +49 5251 60 3855; fax: +49 5251 60 3854.

[3] This steel was developed by Transportation Technology Center Inc. (TTCI), a subdivision of Association of American Railroads (AAR).

0921-5093/$ – see front matter © 2007 Published by Elsevier B.V.
doi:10.1016/j.msea.2007.08.049

conditions, and the observations indicated a similar or reduced wear and fatigue performance compared to that of the aforementioned pearlitic steel [2,4], prompting a closer look at the finite deformation mechanisms at ~~large-plastic~~ strains. The 1% C rail steel is another pearlitic rail steel, which was considered in the current work for the verification of the modeling approach taken.

Another contribution of the work presented herein is the development of a methodology to obtain information on stress–strain-texture states of steels at ~~large-plastic~~ strains (exceeding 1.0) beyond the capabilities of standard laboratory experiments. The modified visco-plastic self-consistent (VPSC) model that accounts for the specific details of the bainitic and pearlitic microstructures was used to predict the shear strain hardening response and yield strength in shear, based on only the materials' response under uniaxial tensile loading and their initial textures. The objective was to obtain a material's deformation response and the corresponding texture evolution simultaneously through a single VPSC simulation, eliminating additional experimental observations that are both time wise and financially demanding in comparison to numerical simulations.

The proposed method utilizes crystal plasticity concepts establishing the link between deformation mechanisms at the microstructural level, and mechanical properties. The link between the tensile deformation mode, and the shear and compressive responses is established by considering the anisotropy of the materials. This requires the incorporation of deformation mechanisms of the materials under investigation. All three materials considered in this study (J6 bainitic steel, pearlitic steel, and 1% C rail steel) possess a bcc lattice structure with different types of strengthening secondary phases, which alone requires the theoretical consideration of the complexity of the slip mechanism related to the bcc structure. Experimental observations have shown that slip takes place on the $\{1\,1\,0\}$, $\{1\,1\,2\}$ and $\{1\,2\,3\}$ planes and in the $\langle 1\,1\,1\rangle$direction in bcc crystals [5,6]. Of these the $\{1\,1\,0\}$ plane is the most nearly close-packed, making it the primary slip plane in bcc materials. As mentioned previously by Havner [5], one noteworthy observation regarding the finite deformation of bcc crystals is that there are few works on slip in bcc crystals since Taylor and Elam's early works [7–9]. In this work, we provide simulations over a ~~large-strain~~ regime for two rather different microstructures allowing slip on $\{1\,1\,0\}$ based systems.

Similar to slip, texture evolution is another topic that has not been extensively studied in bcc materials. A large fraction of the texture literature deals with rolling of face-centered cubic (fcc) metals [10]. Nevertheless, the literature contains studies that attempted to investigate the relationship between slip activity and texture evolution in bcc materials [11–13], most of which concentrate on the role of pencil glide on the texture evolution. The work of Rollett and Kocks [11] demonstrated that the texture development in tension was essentially the same as for restricted glide (the $\{1\,1\,0\}\langle 1\,1\,1\rangle$ slip), whereas significant differences surfaced in plane strain compression. In the light of this finding, all possible combinations of slip activity were allowed in the preliminary simulations, yet no drastic differences were revealed neither in the deformation response nor the texture evolution. Thus, in the current work, only primary slip is considered as the means of plastic deformation, and therefore the 12 $\{1\,1\,0\}\langle 1\,1\,1\rangle$ slip systems were allowed in the corresponding simulations.

In this study two unique strain hardening formulations are proposed that account for the fine features of pearlitic and bainitic microstructures, and simulations are presented for stress–strain response and texture evolution in bcc crystals. The texture evolution in bcc steels at strains within the experimental range of standard laboratory equipment and at higher strains is investigated to illustrate the trends. Texture evolution is utilized as a tool for determining the state of stress in rails taken from service in an inverse fashion. Specifically, the changes in normalized texture intensities of specific crystallographic orientations are monitored. It is also shown that the use of an isotropic yield criterion, such as the von Mises criterion (as commonly adopted in finite element codes), has limitations where the degree of texture increases with the applied deformation. The anisotropy of a material is manifested through the "Taylor factor" calculated. Our proposed approach incorporates volume fraction of lamellae, and its orientation change upon deformation at large strains. The transmission electron microscopy observations provide a measure of the length scales associated with the secondary phases. The work provides improved understanding of deformation in bcc materials where texture evolution is evident in the presence of a secondary phase.

2. Experimental techniques

Three different rail steels were investigated in this study: bainitic steel (BS), pearlitic steel (PS) and 1% C rail steel (1CRS). The bainitic steel has 0.26% C, 2.0% Mn, 1.81% Si, and 1.93% Cr, while the ladle analysis for both pearlitic steels yielded 0.91% Mn, 0.66% Si, 0.47% Cr, and 0.79% C for the PS and 1.0% C for the 1CRS.[4] All three materials have a bcc structure at room temperature. The specimens for all three loading scenarios (tension, compression and torsion) were extracted from rail heads, such that the loading axis of each sample on the test frame coincides with the rolling direction of the rails (Fig. 1). Small-scale samples were utilized for tension (dog-bone shaped, with a gauge length of 10 mm) and compression (prismatic, with a cross-section of 16 mm^2) tests, whereas large-scale tubular specimens (with a gauge section of 30 mm in length and a wall thickness of 1.4 mm) were used for pure torsion tests.

Uniaxial tension and compression experiments were conducted as the first step in mechanical testing with the purpose of defining the fundamental macroscopic properties of the materials. The strain hardening response is also closely monitored with the aid of these tests. However, owing to the small amount of ductility in tensile tests and relatively narrower strain span studied, experiments under compression, as well as shear experiments, were also carried out. The torsion test was conducted as it represents the simplest experimental method of obtaining simple shear deformation. Such tests are very useful for obtaining strain hardening data for ~~large-plastic~~ strains (exceeding 1.0)

[4] The compositions provided reflect weight percentage.

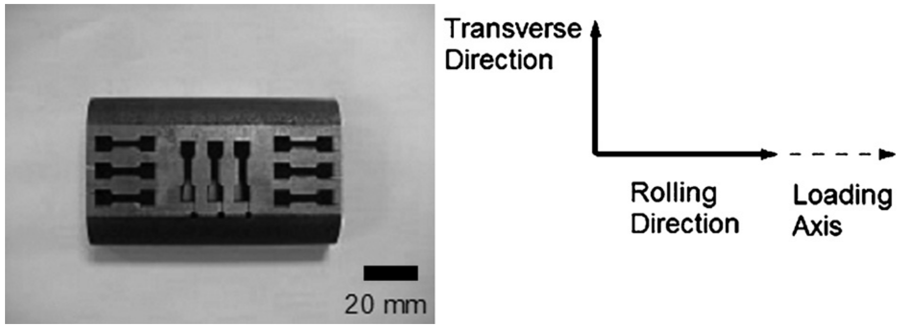

Fig. 1. All the specimens reported on in the present study were extracted from rails in such a way that their loading axis on the test frame coincides with the rolling direction (i.e. the longitudinal direction of the rail). Only extraction of tensile specimens is shown. The rail head is shown from the top.

avoiding the friction effects at interfaces between specimens and platens that occur in compression testing [10] or early facture in tension experiments.

The experiments were conducted at quasi-static strain rates, namely at an initial rate of $4 \times 10^{-4}\,s^{-1}$. ~~The~~ strain rate was chosen with the purpose of establishing the mechanical properties where strain rate dependence would not be pronounced [14]. Tests for each loading type were checked for repeatability. Servo hydraulic load frames equipped with digital controllers were utilized in conducting the mechanical tests. Miniature extensometers were used to accurately measure the strain on the sub-sized tensile and compressive samples.

The textural changes were monitored through X-ray diffraction (XRD). The experimental data obtained from XRD or the texture information obtained as an output from the simulations were interpreted with the aid of the Preferred Orientation Package (popLA) developed at the Los Alamos National Laboratory [10]. For each case, at least three experimental pole figure measurements were taken with XRD as this is the minimum number of different poles to construct an orientation distribution function (ODF). ODF is the most complete description of a texture in three-dimensional space. As a general rule, three or more pole figure data points are needed that correspond to each orientation distribution (OD) cell computed by discrete methods [10]. Our experimental data was obtained through three measurements for each sample: (1 1 0), (2 0 0), and (2 1 1) poles. These are the poles that exhibited the peak intensities during the initial θ–2θ scan.

The ODFs for the experimentally measured textures and inverse pole figures were calculated using popLA. The numerically predicted textures, on the other hand, were given by the current model in the form of Euler angles that represent the texture in the form of orientations assumed by individual grains. The corresponding ODFs and inverse pole figures were calculated utilizing popLA.

Complimentary microstructural observations were conducted through transmission electron microscopy (TEM), which was utilized to investigate the microstructural mechanisms such as dislocation activities or slip systems, in addition to showing the initial microstructural status of the complex industrial alloys studied (Fig. 2). The difference between the microstructures of the two-phase alloys studied is evident from the representative microscopy images presented in Fig. 2: (a) bainitic structure for BS and (b) pearlitic structure for PS. The fine lamellar structure is evident in the case of PS, and for BS the TEM observations indicate the presence of fine precipitates.

Having the microstructural information as a background facilitates the construction of the hardening rules. We then place the focus of this study on modeling the macroscopic deforma-

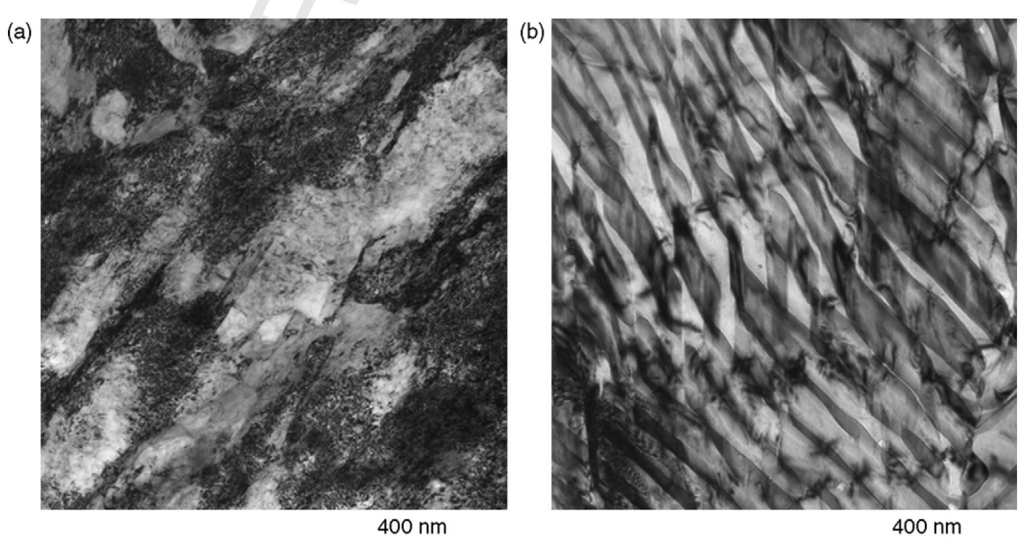

Fig. 2. Representative TEM images showing the initial microstructure of the materials studied: (a) bainitic and (b) pearlitic steels.

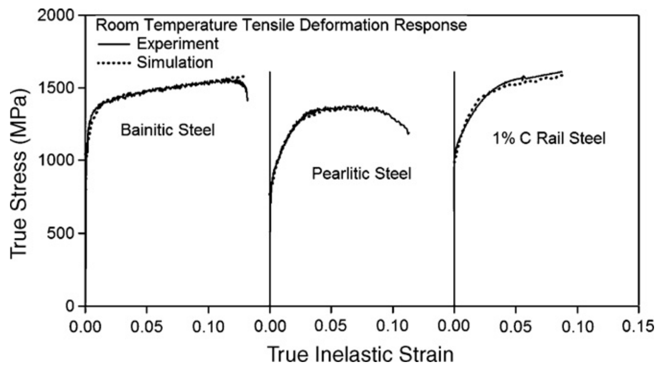

Fig. 3. Room temperature tensile deformation response and the corresponding simulation results for BS, PS, and 1CRS. All experiments ended with the failure of the specimens. The experimental curves represent average of several individual experiments carried out for each case. Simulations do not extend beyond the ultimate tensile strength levels.

tion response of the materials studied, and the corresponding texture evolution.

3. Tensile deformation response and its modeling

The room temperature tensile stress–strain responses of all three materials studied are reported in Fig. 3. The materials in consideration exhibit a limited amount of ductility (0.13, 0.12 and 0.095 plastic strain for BS, PS and 1CRS, respectively), which is not very surprising for this class of high-strength alloys. In order to model the deformation response of the materials studied (Fig. 3), the VPSC algorithm originally developed by Lebensohn and Tomé [15] was modified to account for relevant microstructural details of the different steels and employed as the numerical tool. This particular algorithm was chosen based on several reasons. First of all, both literature and our experience have proven the capability of VPSC to effectively model the deformation response of high-strength steels with complex deformation mechanisms [14] both in single crystal and polycrystalline form. More importantly, VPSC captures the texture evolution during deformation and gives the opportunity to assign the experimentally determined pre-deformation texture of the material as the starting state, which is crucial for obtaining realistic results. The model also enables incorporation of experimentally observed additional microstructural features into the numerical algorithm with ease and efficiency [14].

We present the fundamentals of the original VPSC algorithm in order predict deformation response in the plastic regime. Plastic deformation occurs when a slip or a twinning system becomes active. The resolved shear stress, τ_{RSS}^{s}, for a system (s) is given by

$$\tau_{\mathrm{RSS}}^{s} = m_i^s \sigma_i \tag{1}$$

where m_i^s is the vector form of the Schmid tensor and σ_i is the vector form of the applied stress. To describe the shear rate in the system s, a non-linear shear strain rate as a power of τ_{RSS}^{s} is written as

$$\dot{\gamma}^s = \dot{\gamma}_0 \left(\frac{\tau_{\mathrm{RSS}}^{s}}{\tau_0^s}\right)^n = \dot{\gamma}_0 \left(\frac{m_i^s \sigma_i}{\tau_0^s}\right)^n \tag{2}$$

where $\dot{\gamma}_0$ is the reference rate, τ_0^s the threshold stress corresponding to this reference rate, and n is the inverse of the rate sensitivity index. If n is high enough, this description asymptotically approaches the rate-insensitive limit. The total strain rate in a crystal can be written as the sum of contributions from all potentially active systems and can be pseudolinearized as follows [15]:

$$\dot{\varepsilon}_i = \left[\dot{\gamma}_0 \sum_1^s \frac{m_i^s m_j^s}{\tau_0^s}\left(\frac{m_k^s \sigma_k}{\tau_0^s}\right)^{n-1}\right]\sigma_j = M_{ij}^{\mathrm{c(sec)}}(\tilde{\sigma})\sigma_j \tag{3}$$

where $M_{ij}^{\mathrm{c(sec)}}$ is the secant visco-plastic compliance of the crystal which gives the instantaneous relation between stress and strain rate.

Following Lebensohn and Tomé [15], at the polycrystal level the same pseudolinear form can be implemented as in the case of Eq. (3) as follows:

$$\dot{E}_i = M_{ij}^{(\mathrm{sec})}(\tilde{\Sigma})\Sigma_j + \dot{\Sigma}^0 \tag{4}$$

where $\dot{E}_i$ and Σ are the polycrystal strain rate and applied stress.

In a continuum that consists of a matrix and inclusions, the deviations in strain rate and stress between the inclusion and their overall magnitudes are defined as

$$\dot{\tilde{\varepsilon}}_k = \dot{\varepsilon}_k - \dot{E}_k \tag{5}$$

$$\tilde{\sigma}_j = \sigma_j - \Sigma_j \tag{6}$$

where $\dot{\varepsilon}_k$ and σ_j stand for the local (single crystal or grain level) strain rate and stress. Utilizing Eshelby's inhomogeneous inclusion formulation one can solve the stress equilibrium equation to derive the following interaction equation [10]:

$$\dot{\tilde{\varepsilon}} = -\tilde{M} : \tilde{\sigma} \tag{7}$$

The interaction tensor $\tilde{M}$ is defined as

$$\tilde{M} = n'(I - S)^{-1} : S : M^{(\mathrm{sec})} \tag{8}$$

where $M^{(\mathrm{sec})}$ is the secant compliance tensor for the polycrystal aggregate and S is the visco-plastic Eshelby tensor [10].

The macroscopic secant compliance, $M^{(\mathrm{sec})}$, can be determined by substituting Eqs. (3) and (4) in Eq. (7). The macroscopic strain rate is evaluated by taking the weighted average of crystal strain rates over all the crystals as follows:

$$M^{(\mathrm{sec})} = \langle M^{\mathrm{c(sec)}} : (M^{\mathrm{c(sec)}} + \tilde{M})^{-1} : (M^{(\mathrm{sec})} + \tilde{M})\rangle \tag{9}$$

Iterative solution of Eqs. (3), (7) and (9) gives the stress in each crystal (grain), the crystal's compliance tensor, and the polycrystal compliance consistent with the applied strain rate $\dot{E}_i$. In this work, we chose the term n (in Eq. (2)) to be in the rate insensitive limit ($n = 20$). As for the interaction equation (8), an effective value of $n' = 1$ is used, which ensures a rigid interaction [15,16].

The rate of overall dislocation density can be expressed as

$$\dot{\rho} = \sum_n \{k_1\sqrt{\rho} - k_2\rho\}|\dot{\gamma}^n| \tag{10}$$

Please cite this article in press as: D. Canadinc, et al., Mater. Sci. Eng. A (2007), doi:10.1016/j.msea.2007.08.049

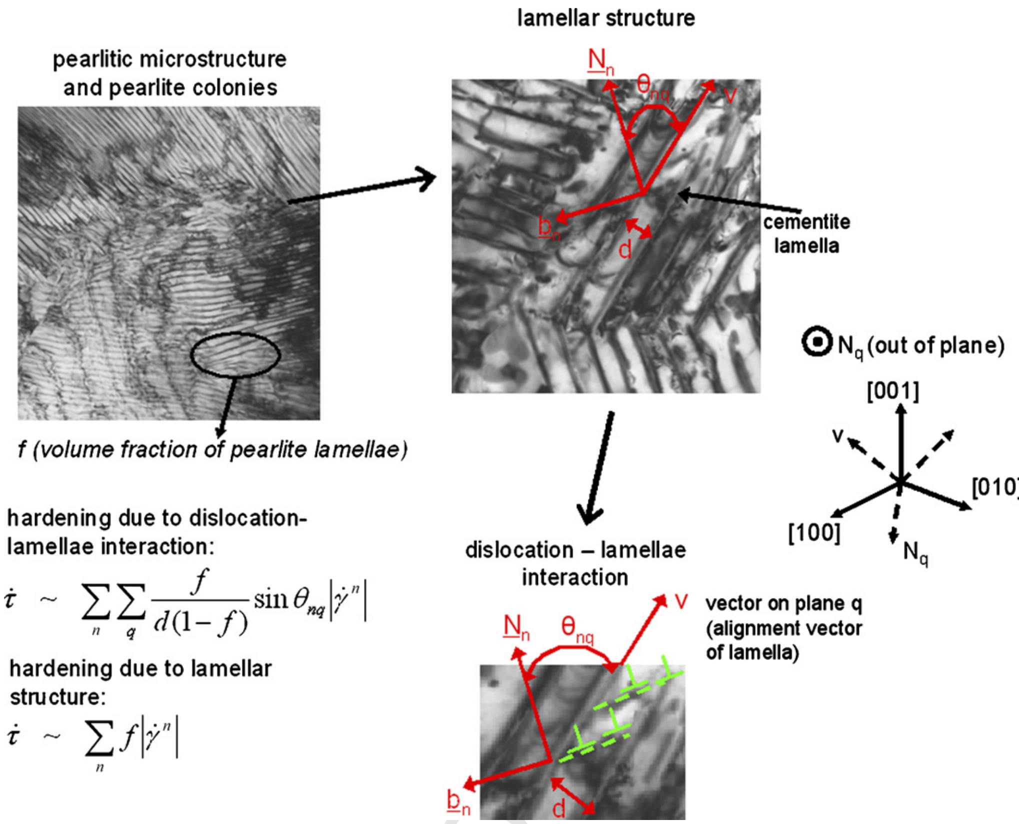

Fig. 4. Schematic showing the incorporation of the contribution of interaction between pearlite lamellae and glide dislocations into the Voce hardening scheme. See Eq. (20) for details.

where k_1 and k_2 are the geometric constants that define the athermal (statistical) storage of the moving dislocations [10].

We define the flow stress τ in the traditional Taylor hardening format as

$$\tau - \tau_0 = \alpha\mu b\sqrt{\rho} \tag{11}$$

where α is the dislocation interaction parameter and τ_0 is a reference strength, which is related to deformation at the grain level as will be detailed later on. From Eq. (11), with τ_0 constant, the rate of the flow stress is obtained by taking the time derivative as

$$\dot{\tau} = \frac{\alpha\mu b\dot{\rho}}{2\sqrt{\rho}} \tag{12}$$

Substituting Eq. (10) into Eq. (12) results in

$$\dot{\tau} = \sum_n \left\{ k_1 \frac{\alpha\mu b}{2} - k_2 \frac{\alpha\mu b}{2}\sqrt{\rho} \right\} |\dot{\gamma}^n| \tag{13}$$

From Eq. (11), the following identity is obtained for the square root of the density of dislocations:

$$\sqrt{\rho} = \frac{\tau - \tau_0}{\alpha\mu b} \tag{14}$$

Once Eq. (14) is substituted into Eq. (13), the rate of flow stress evolution is given by:

$$\dot{\tau} = \sum_n \left\{ k_1 \frac{\alpha\mu b}{2} - k_2 \frac{\tau - \tau_0}{2} \right\} |\dot{\gamma}^n| \tag{15}$$

One should note that the term $\{(\alpha\mu b/2)k_1 - ((\tau - \tau_0)/2)k_2\}$ in Eq. (15) is the linear Voce hardening term (Eq. (17)). Having noted this, Eq. (15) can also be expressed as [10,16]:

$$\dot{\tau} = \sum_n \left\{ \theta_0 \left(\frac{\tau_s - \tau}{\tau_s - \tau_0} \right) \right\} |\dot{\gamma}^n| \tag{16}$$

where θ_0 is the constant strain hardening rate, and τ_s represents the saturation stress in the absence of geometric effects, or the threshold stress. The hardening is defined by an extended Voce law [10,14,16], which is characterized by the evolution of the threshold stress (τ^s) with accumulated shear strain (Γ) in each grain of the form:

$$\tau^s = \tau_0 + (\tau_1 + \theta_1\Gamma)\left(1 - \exp\left(-\frac{\theta_0\Gamma}{\tau_1}\right)\right) \tag{17}$$

where τ_0 is the reference strength, and τ_1, θ_0 and θ_1 are the parameters that define the hardening behavior [10,16]. The hardening law defined by Eq. (17) characterizes the onset of plasticity and the saturation of threshold stress at larger strains. The general conditions of $\theta_0 \geq \theta_1 \geq 0$ and $\tau_1 \geq 0$ need to be fulfilled for positive hardening, whereas $\theta_0 \leq \theta_1 \leq 0$ and $\tau_1 \leq 0$ should be satisfied simultaneously for describing negative hardening. The limit case of the Voce hardening law, namely linear hardening, takes place when $\tau_1^s = 0$.

VPSC follows the algorithm outlined in Eq. (1) through (17) and solves for the stresses corresponding to the given strains throughout the deformation. The self-consistent algorithm is solved with three nested iterations [16]. Briefly, the outer iteration varies the stress and the compliance in each grain. The intermediate iteration varies the overall tangent modulus of the aggregate (see Ref. [17] for more details), whereas the inner iteration varies the overall secant compliance.

3.1. Incorporation of the pearlitic microstructure into the VPSC algorithm

At this point, the authors would like to point at two possibilities regarding modeling with VPSC. The first is to use the VPSC in its original form for carrying out simulations, which would return satisfactory fits for all cases. However, we note that this approach basically means disregarding the differences between the microstructures of pearlitic and bainitic steels and does not account for the variation in microstructural constituents, and thus, the predictive capabilities would be rather limited. In order to present a more realistic approach, we chose to incorporate the relevant microstructural features of pearlitic and bainitic microstructures into the VPSC algorithm.

The pearlitic microstructure possessed by PS and 1CRS features cementite lamellae inside the pearlite colonies. Upon initial cooling of the steel, in each austenite grain, the pearlite lamellae starts to grow in a particular direction at a specific nucleation site. Eventually, the grain interiors are occupied by a lamellar structure that is made of “colonies” of lamellae grown in certain directions (Fig. 4). The corresponding orientation of the lamellae depends on the orientation of the grains and the positioning of the grain boundaries, which directly affect the nucleation of the lamellae during the initial cooling of the steel. In a microstructure with a (nearly) random texture, however, it is reasonable to assume that the lamellar cells also represent a random orientation distribution over the whole aggregate.

It is very well known that the lamellae (made of Fe_3C) constitute hard microstructural barriers, which have a substantial influence on the mechanical properties of pearlitic steels. In the current study, we incorporate the length scales associated with the pearlite lamellae into the Voce hardening formulation to capture the role of the pearlitic microstructure on the deformation response. Specifically, we consider the pearlite lamellae as impenetrable and to constitute obstacles against dislocation glide on the active slip systems (Fig. 4).

In previous studies [14,18,19] we modeled the contribution of high-density dislocation walls (HDDWs) to the overall hardening by utilizing a unique strain hardening formulation. Specifically, we modeled the HDDWs as impenetrable walls that form obstacles to dislocation motion, but also evolve in volume fraction as a result of this interaction with glide dislocations. Moreover, the model also takes into account the reorientation of HDDWs due to plastic deformation. In the current study, we treated pearlite lamellae similar to HDDWs, yet with important differences. In particular, the pearlite lamellae are modeled as impenetrable elongated inclusions that reorient in the matrix due to plastic deformation, however, as opposed to HDDWs, they do not evolve in volume fraction due to interaction with glide dislocations.

The present model utilizes a crystal plasticity description of the strain rate at the single crystal level, and the reference stress evolves with the dislocation density. The pearlite lamellae–glide dislocation system interaction is incorporated into the overall rate of dislocation density, such that Eq. (10) becomes

$$\dot{\rho} = \sum_n \{k_1\sqrt{\rho} - k_2\rho\}|\dot{\gamma}^n| + \sum_n\sum_q \frac{K}{db}\sin\theta_{nq}|\dot{\gamma}^n| \tag{18}$$

where K is a geometric constant, and b represents the ~~burgers~~ vector [14,18–20]. The first term $\sum_n\{k_1\sqrt{\rho} - k_2\rho\}|\dot{\gamma}^n|$ represents the athermal (statistical) storage of moving dislocations ($k_1\sqrt{\rho}$) and dynamic recovery ($-k_2\rho$) [20], whereas the second term $\sum_n\sum_q(K/db)\sin\theta_{nq}|\dot{\gamma}^n|$ accounts for the contribution due to pearlite lamellae formed parallel to a plane q acting as effective obstacles to the moving of dislocations gliding on the active slip system n (Fig. 4). In other words, the second term represents a phenomenological geometric accumulation of dislocations at the boundaries of pearlite lamellae, which subdivide the grains (and the lamellar cells within the grains) and thereby decrease the mean free path of dislocations [20]. The angle θ_{nq} is the angle between the direction of slip in the active slip system n and the direction of pearlite lamellae on (or parallel to) the plane q, and is incorporated as a measure of the interaction between pearlite lamellae and glide dislocations in a geometric sense. The angle θ_{nq} is a variable, such that it can take different values depending on the active slip systems and the orientation of pearlite lamellae they interact with. Moreover, the θ_{nq} continues to change as the deformation progresses due to the rotation of the lamellae in the matrix. The term d represents the average spacing between the lamellae. The term $\dot{\gamma}^n$ stands for the rate of shear in the active slip system n. The lamellae are treated as impenetrable barriers to dislocation motion, acting as hard phases in the matrix, similar to precipitates. Accordingly, they are modeled as (elongated) ellipsoidal inclusions in the matrix. As plastic strain progresses, Orowan loops are stored at the interfaces of the pearlite lamellae, giving rise to long-range internal stresses in the matrix [20]. This additional hardening (τ^{B}) due to pearlite lamellae acting as hard phases in the matrix is included through the term:

$$\tau^{\mathrm{B}} = 2f\xi\mu\sum_n|\gamma^n| \tag{19}$$

where the terms μ, ξ, and f stand for the shear modulus, the Eshelby accommodation factor for elongated ellipsoidal inclusions [14], and the volume fraction of HDDWs, respectively. The $\sum_n\gamma^{(n)}$ term is simply the summation of the shear strains on the active slip systems and represents the total matrix mismatch strain brought about by the pearlite lamellae. The volume fraction of cementite (or impenetrable lamellae) (f) is a constant, and taken as 0.4 in the current study. Following the incorporation of the additional hardening terms due to the pearlite lamellae,

Please cite this article in press as: D. Canadinc, et al., Mater. Sci. Eng. A (2007), doi:10.1016/j.msea.2007.08.049

the original rate of flow stress $\dot{\tau}$ defined in Eq. (16) becomes

$$\dot{\tau} = \sum_n \left[\frac{\alpha^2 \mu^2 b K}{4d(\tau - \tau_0)} \frac{f}{1-f} \sum_q \sin\theta_{nq} + 2f\xi\mu + \left\{ \theta_0 \left(\frac{\tau_s - \tau}{\tau_s - \tau_0} \right) \right\} \right] |\dot{\gamma}^n| \quad (20)$$

In order to represent the orientation of pearlite lamellae in three-dimensional space and account for their geometric interaction with the glide dislocations, we assumed that the texture also reflects the orientation distribution of the pearlite lamellae. For this purpose, the plane q that the pearlite lamellae form on or parallel to was taken as the plane, the normal of which is the orientation vector of the corresponding grain (Fig. 4). Accordingly, we adopt the following convention: the pearlite lamellae are assigned a single orientation in each grain, such that the longitudinal axis of each lamella in the corresponding grain coincides with or is parallel to a vector $\underline{v}$ on plane q with a plane normal $\underline{N}_q$. The relationship between $\underline{v}$ and $\underline{N}_q$ is such that they form the two of the three axes of a local frame. For instance, if $\underline{N}_q$ is the [1 0 0] unit vector in the reference frame, then $\underline{v}$ would be in the [0 0 1] direction of the reference frame (Fig. 4). Thus, for each grain, the necessary rotation for the [1 0 0] unit vector of the reference frame to coincide with the surface normal was calculated, and then applied to the [0 0 1] axis of the reference frame. This approach was basically chosen in order to assign orientations to pearlite lamellae in each grain in a consistent manner, and thereby describe the geometric relationship between cementite lamellae and glide dislocations in the reference frame.

Finally, the reorientation of pearlite lamellae was accomplished by adopting a scheme similar to the twin reorientation scheme in VPSC. Specifically, the pearlite lamellae were rotated due to plastic deformation within a grain. This was accomplished by representing the calculated lamellar orientations in terms of Miller indices and having the reorientation scheme determine the rotation imposed by plastic deformation. In our previous studies [14,18,19] we successfully accounted for the rotation of HDDWs in Hadfield steel single and polycrystals utilizing the same approach.

3.2. Incorporation of the bainitic microstructure into the VPSC algorithm

In a previous study [20] we successfully modeled the role of precipitation hardening on the deformation response of nitrogen-alloyed Hadfield steel single crystals. In the current work, we adopted the strain hardening formulation developed previously [20]. In the present approach, we consider the carbides within the bainite modifying the critical shear stress on the slip systems, similar to precipitates (Fig. 5). This is achieved by modifying the Voce hardening formulation (Eq. (16)) accounting for the dislocation–particle interaction and by considering the particles as one of the controlling factors of the mean free path of dislocations. As plastic strain progresses, Orowan loops are stored around the precipitates, which gives rise to long range internal stresses in the matrix. The back stress evolves rapidly at the

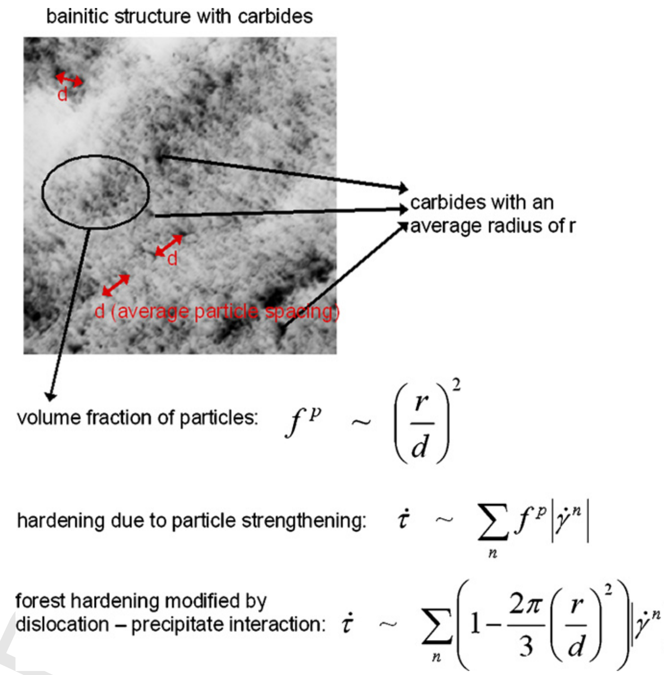

Fig. 5. Schematic showing the incorporation of the contribution of particle strengthening into the Voce hardening scheme. See Eq. (25) for details.

beginning of deformation but tends to saturate with increasing strain due to plastic relaxation mechanisms around the particles during deformation, such as formation of prismatic dislocation loops, and dislocation annihilation. We treat semi-coherent and incoherent particles as elastic inclusions and follow a formulation initially similar to Bate et al. [21], Brown and co-workers [22–24] and Barlat and Liu [25]. The exact formulation differs in details as we also incorporate geometric storage of dislocations as a contribution to the forest hardening.

Assuming that the aggregates of carbides are elastic inclusions in the matrix, applying a uniform strain to the body that is associated with a stress, τ^{m}, gives the overall stress as

$$\tau = (1 - f)\tau^{\mathrm{m}} + f\tau^{\mathrm{p}} \quad (21)$$

where τ^{p} is the stress due to the carbides within the bainite, f the volume fraction of precipitates, and τ^{m} is the shear stress in the matrix.

Considering the Eshelby inclusion problem, τ^{p} can be written as

$$\tau^{\mathrm{p}} = C(I - S)\gamma_{\mathrm{p}} \quad (22)$$

where I and S are the fourth order identity and Eshelby tensors, respectively, C the elastic modulus tensor and γ_{p} is the plastic strain discontinuity at the matrix/particle interface. Technically, the value of the strain discontinuity should be less than the applied strain due to plastic relaxation around the particle after a certain amount of strain. Eq. (22) can be written for spherical inclusions as [26]:

$$\tau^{\mathrm{p}} = 2\mu\chi D\gamma_{\mathrm{p}}^{*} \quad (23)$$

where χ is the Eshelby accommodation factor, μ the shear modulus, D is the modulus correction term and * represents the unrelaxed portion of the plastic strain. D is orientation dependent because of the orientation dependency of the single crystal moduli.

The anisotropy due to the precipitates is incorporated into the model by the magnitude of the accommodation factor, which is dependent upon the shape and orientation of the precipitates. The term $f^{\mathrm{p}}\tau^{\mathrm{p}}$ opposes the applied stress during the deformation, resulting in a back stress. The back stress evolves with increasing strain and tends to saturate due to plastic relaxation. Brown and Stobbs [24] demonstrated that the plastic relaxation strain is a function of the applied strain level, and the precipitate size, shape and volume fraction, and can be approximated for spherical precipitates as

$$\gamma_{\mathrm{p}}^{*} = \left(\frac{8\pi b}{\alpha^2 \gamma_{\mathrm{p}} r_0}\right)^{1/8} \alpha \left(\frac{8\gamma_{\mathrm{p}} b}{\pi r_0}\right)^{1/2} \tag{24}$$

where r_0 is the radius of particles. The first term in Eq. (21) is the stress in the matrix, which depends upon the internal state variable, the dislocation density, and can be found by using Eq. (16). Replacing Eq. (16) and the time derivative of Eq. (24) into the time derivative of Eq. (21) results in the constitutive relation for stress evolution with plastic relaxation around particles:

$$\dot{\tau} = \left[\left(1 - \frac{2\pi}{3}\frac{r^2}{d^2}\right)\theta_0 \left\{\frac{\tau_s - \tau}{\tau_s - \tau_0}\right\} + \pi\chi\frac{r^2}{d^2}\mu D A \frac{1}{\gamma^{5/8}}\right] \sum_n |\dot{\gamma}^n| \tag{25}$$

In Eq. (25), the term d represents the average distance between carbides in the bainite. A is a derived parameter, which is a function of the carbides and the inter-particle distance [20]. Ideally, the volume fraction of particles depends on the radius of particles and the distance between particles (Fig. 5), $f^{\mathrm{p}} = (2\pi/3)(r/d)^2$ [27]. In this case, we take the volume fraction of the carbides in the bainite as 0.4.

3.3. Simulations

We modeled the room temperature uniaxial tensile deformation response of all three materials under investigation (Fig. 3). Only primary slip, namely slip on the $\{1\,1\,0\}\langle 1\,1\,1\rangle$ system, was considered as the means of plastic deformation during simulations, as at the temperatures considered iron-based bcc materials tend to deform predominantly by slip activity on $\{1\,1\,0\}$ planes [28]. The initial textures measured experimentally via XRD were used as an input defining the initial state of the microstructure. Temperature and rate sensitivity were not taken into account, considering that the deformation takes place at low homologous (room) temperature and a slow strain rate.

The critical step in the modeling of the deformation response is the determination of the hardening parameters that define the plastic flow during straining. To claim any success for the modeling effort presented herein, the parameters must be physically meaningful, in addition to providing a good prediction of the experimental data. There are four parameters to be determined, namely the Voce hardening parameters τ_0, τ_1, θ_0 and θ_1.

Table 1
Voce hardening parameters defining the room temperature deformation responses of all three materials under uniaxial tensile, torsional and uniaxial compressive loadings

	τ_0 (MPa)	τ_1 (MPa)	θ_0 (MPa)	θ_1 (MPa)
BS	373	355	2.0×10^4	233
PS	275	413	1.0×10^3	37
1CRS	356	358	1.1×10^3	239

For a polycrystalline material with grains assuming various orientations in 3D space, the determination of the microscopic yield strength (τ_0), or the critical resolved shear stress (CRSS), is not as straightforward as it is for a single crystal, which is governed by the Schmid's Law. In reality, for each grain, depending on the orientation it assumes, the effective stress imposed on that grain will change, bringing about a different yield point compared to grains oriented differently. An early solution to this problem was proposed by Sachs, who postulated that the microscopic yield point of a polycrystalline aggregate could be represented by the average of critical resolved shear stresses of all grains in the aggregate [29]. However, this is a rather oversimplifying approach, as pointed out by Taylor, cf. Hosford [29].

In the present study, the determination of the microscopic yield strength for the polycrystalline aggregate was carried out with the aid of simulations, however, based on Taylor's analysis [29,30]. The reference strength τ_0 for each material was determined such that the values chosen lead to the correct onset of the plastic regime, and therefore the accurate macroscopic yield strength level for the tensile deformation response. In order this determination process not to be trivial, we started with an initial guess based on Bishop and Hill's work [30]. A simple algorithm [31] was written based on this work that takes the experimentally determined initial textures into account to reflect the level of anisotropy possessed by each material, and calculates the corresponding Taylor factor. Accordingly, the initial guess for τ_0 is related to the macroscopic yield strength (σ_y) (in a similar fashion to the Schmid's Law) through the Taylor factor (M) as

$$\tau_0 M = \sigma_y \tag{26}$$

This initial guess of τ_0 is modified as necessary to accommodate the correct predictions of the macroscopic yield strength level and the onset of the plastic regime for each material while predicting the tensile stress–strain response. Once the reference strength τ_0 was determined for each material, the other parameters were established by simply trying to predict the (post-yield) experimental hardening behavior displayed under tensile loading, following the guidelines for the Voce hardening law. The parameters utilized to predict the room temperature stress–strain response of the three materials under investigation are given in Table 1. Utilizing these parameters, the current model successfully simulated the tensile deformation response for all three materials (Fig. 3).

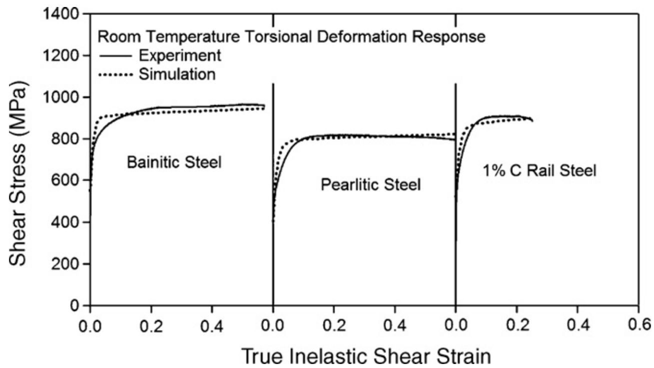

Fig. 6. Room temperature torsional deformation response and the corresponding simulation results for BS, PS, and 1CRS. All experiments ended with the failure of the specimens.

4. Predicting the shear response and the yield strength in shear

The most reliable way of determining the shear response of a material is basically a pure torsion test conducted on a specimen of the same material. However, when it comes to a full or extensive characterization of a new material, many factors, such as macroscopic properties, microstructure, and texture are involved. Experimental investigation of all these aspects not only means spending considerable amount of time and effort performing various laboratory tests, but it also restricts the results to the boundaries dictated by the strain values that are attainable in the laboratory.

Utilizing the current model we aim to effectively establish some of the important characteristics of a material based on much less experimental effort. In what follows, a method for numerically predicting the shear yield strength in shear and stress–strain response and texture evolution under shear loading is outlined. One way of predicting the yield strength and deformation response in shear based on the tensile deformation response is to utilize a yield criterion, such as the von Mises and Tresca yield criteria [32]. However, these yield criteria provide a quick and good estimate of the shear yield strength based on the macroscopic tensile yield strength for engineering applications, only under the assumption of the material being isotropic. Even then it has been shown that they fall short of reflecting the correct form of the yield potential [29,30], and the differences become more pronounced when anisotropy is present [30].

An alternative and better way is to relate all different deformation modes at the macroscopic level to the microscopic deformation at the grain (or single crystal) level. At this point, the capability of predicting the deformation response for any given deformation relies only on correctly modeling the material's response at the microscopic level. This was outlined and achieved in the previous section while modeling the tensile deformation response of the three materials. No matter what the imposed macroscopic deformation mode is, at the grain level, the deformation in a single crystal on any slip system is carried out through shearing. Therefore, the hardening parameters relating the microscopic deformation mechanisms to the macroscopic tensile deformation response are expected to successfully capture stress–strain behavior displayed under any other imposed deformation mode.

Table 2
Yield strength in shear: comparison of experimentally determined and numerically predicted values

	Yield strength in shear (MPa)	
	Experimental	Predicted
BS	575	568
PS	462	450
1CRS	500	514

The shear simulations were carried out based on the hardening parameters determined through the modeling of the tensile deformation response (Table 1). A close prediction of the experimental shear response (Fig. 6) and the yield strength in shear (Table 2) were obtained for all three materials without any modifications to the material parameters. The numerically predicted values matched the experimental ones, with a negligible difference.

5. Further validation—predicting the compressive deformation response

Investigating the correspondence between the simulations and experimental data of compressive stress–strain behavior was utilized as a separate tool of validation for the method utilized. As it is possible to predict the shear response based on experimental tensile stress–strain data, one should also be able to obtain the compressive response the same way. The current model was utilized to check the validity of the method, and predicted the deformation response of all three materials under compressive loading (Fig. 7). Admittedly, the results shown in Fig. 7 represent not as favorable agreement between numerical and experimental data when compared to the previous two cases (tension and torsion). However, the stress levels and the onset of the plastic regime still show a good agreement between the simulations and experiments. One should note that the material parameters used for compression simulations were not adjusted.

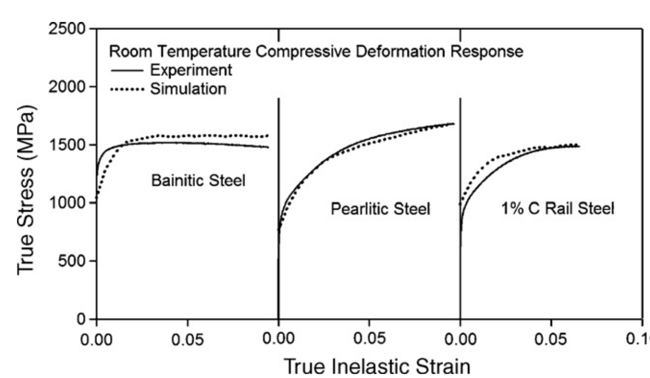

Fig. 7. Room temperature compressive deformation response and the corresponding simulation results for BS, PS, and 1CRS. All experiments ended with the failure of the specimens. Simulations were not extended beyond certain strain levels where buckling initiates.

Please cite this article in press as: D. Canadinc, et al., Mater. Sci. Eng. A (2007), doi:10.1016/j.msea.2007.08.049

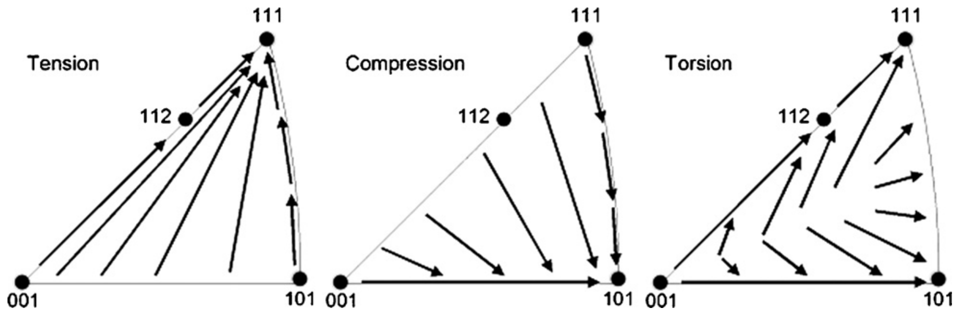

Fig. 8. Stereographic triangle showing the texture evolution in bcc crystals under tensile [5], compressive, and torsional loading.

6. A theoretical study: texture evolution at larger (hypothetical) strains

The amount of ductility available under tensile loading limits the strain span for which we could experimentally observe the texture evolution due to plastic deformation. Similarly, for the torsion tests, due to the nature of the shearing process, it is hard for a preferred or strong texture to develop [10] unless significantly large strains are attained. As for the observation of the compressive response, the results are limited to the strains where instability or buckling initiates.

As a part of the effort to characterize the three materials under investigation, the present study was extended to beyond the practical constraints, and the current model was used to explore the deformation response and accompanying texture evolution at ~~large strains~~ typical of rail applications. BS and PS under torsion were considered for this theoretical investigation. The texture evolution was closely monitored based on the numerical procedure explained earlier.

With regards to the texture evolution in bcc materials, theoretically, slip can take place on three planes: {1 1 0}, {1 1 2}, and {1 2 3} planes, once a bcc crystal is deformed in tension [28]. On all these planes, the slip direction is ⟨1 1 1⟩, giving rise to a change in texture as depicted in Fig. 8 [5,28], which shows that there is a rotation towards the (1 1 1) pole for the tension case. Accordingly, one would expect to see more grains of a bcc polycrystalline aggregate to assume either [1 1 1] or other orientations in the vicinity of [1 1 1] (Fig. 8) as the deformation progresses. In the case of compression of a bcc crystal, however, the rotation is reversed, and takes place toward the (1 0 1) pole (Fig. 8). As for the torsion texture, the rotation of orientations is toward (1 1 1) and (1 0 1) poles, and the (1 1 1)–(1 0 1) boundary. In the present case, neither the experimentally determined nor the corresponding numerically calculated deformation textures revealed such information clearly as the strains practically attainable did not allow its monitoring. However, such effects could be relevant for the actual rails in service. Based on this argument the authors decided to extend the study to hypothetical strains to observe the texture evolution closely as a part of characterization of the current materials.

The present model was utilized to compute the textures at hypothetical shear strains (0–2.0 in torsion) employing the numerical procedure outlined in the previous sections. The texture evolution was monitored for various strain levels within the specified limits for the materials under consideration. Although the widely used inverse pole figures give an idea of the overall picture of the texture evolution due to deformation, they do not present a clear understanding of this evolution in the present case. Therefore, the texture evolution was investigated by monitoring the change in texture intensity of certain orientations ([0 0 1], [1 1 2], [1 1 1] seen in Fig. 8) due to deformation.

With regards to representing the textures, the preference of a crystallographic orientation over the other(s) or a tendency towards a pole in a given texture is most easily represented by "texture intensity". The texture intensity is obtained by the normalization of densities of the orientations (or poles). There exist two ways of normalization: to a value of 1.0 for the average; or to a value of 1.0 for the integral [10]. The former method was utilized throughout this study.

In three-dimensional space, an orientation can be described by three angles Ψ, Θ and Φ, which are the Euler angles [29]. Let (α, β, λ) represent a specific point with α, β and λ corresponding to specific values of Ψ, Θ and Φ in an orientation space represented by the three Euler angles. The total intensity of diffracted X-rays measured at the point (α, β, λ) on an $(h\,k\,l)$ pole figure comes from all crystals (grains) in the sample satisfying the Bragg condition [10]. For the $(h\,k\,l)$ pole, the total pole density from crystals satisfying the Bragg condition is given (in the normalized form) by

$$P_{(h\,k\,l)}(\alpha, \beta) = \frac{1}{2\pi} \int_0^{2\pi} F(\Psi, \Theta, \Phi)\, \mathrm{d}\Gamma \qquad (27)$$

where Γ denotes the path through the orientation distribution (OD) corresponding to rotation about the $(h\,k\,l)$ pole, and F is the OD [10].

It was earlier noted that rotation takes place towards (1 1 1) and (1 0 1) poles, and the (1 1 1)–(1 0 1) boundary in torsion. The general tendency in the current numerical observations agrees with this statement; however, the intensity change of the [1 1 1] orientation is weaker than expected (Fig. 9). The reason for this contradiction could be twofold: the general trend (Fig. 8) is that there is a rotation towards the [1 1 1] orientation (or its vicinity). Still, the shear strains assumed hypothetically (maximum of 2.0) are below the strain levels needed for the intensity of the [1 1 1] orientation to be pronounced. However, one needs to be careful as there is no chance of comparing the hypothetical simulation results with any experimental observations due to the physical constraints. Therefore the investigation of the capability of the proposed method to capture the texture evolution needs further

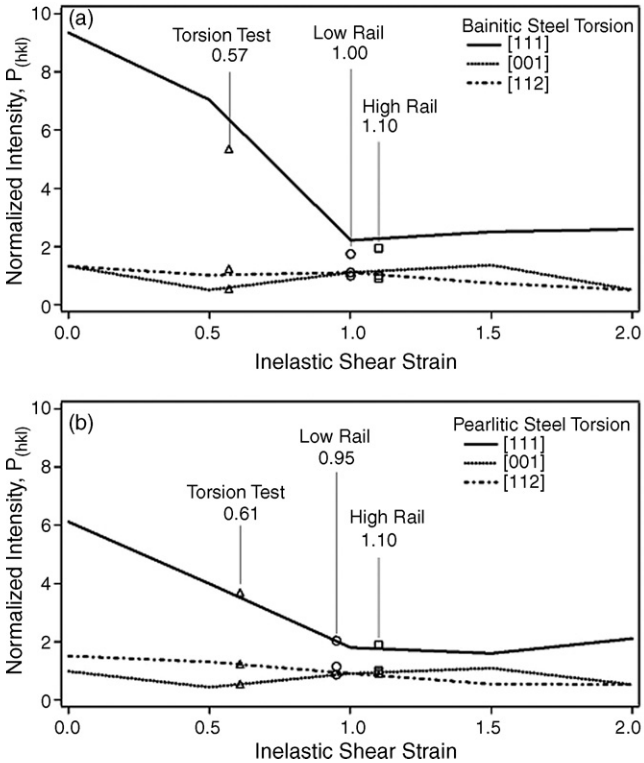

Fig. 9. The "low" and "high" rail textures of (a) BS and (b) PS in comparison with hypothetical torsion simulation results and experimental observations. The fracture shear strain from torsion experiments for both BS (0.57) and PS (0.61) are shown along with the corresponding shear strains for low- and high-rail textures of both materials: 1.00 and 1.10 for BS, and 0.95 and 1.10 for PS.

elaboration, and is well beyond the scope of the work presented herein.

In the real case, where the wheel rolls and slides on the rail, the deformation and the accompanying texture evolution are brought about mainly by shear applied to the surface of the rail. To be able to see where the worn rails stand in terms of texture, the textures of rails taken from service were compared to the ones corresponding to experimental and hypothetical loading scenarios. For this purpose, samples extracted from the "low" and "high" rails of BS and PS underwent XRD. The texture was measured near the contact surface (~~from~~ samples extracted from rails in service), and the data shown was computed for the rolling direction.

The "low rail" is the inner, and the "high rail" is the outer rail of a curved track, and normally, the high-rail wears more than the low rail. Both J6 bainitic and pearlitic steel low and high rails were taken from the test loop with high tonnage: 450 megatonnes (MGT) for BS, and 517 MGT for PS.

The comparison between the experimentally measured textures of the rails and the hypothetical simulation textures was carried out in terms of texture intensities, as the latter reflect the texture evolution in a larger strain span. The comparison was made utilizing the torsion textures, which reflect the simple shear response of the material. Simple shear could be considered as a "close representation" of the real case, where shear is the dominant deformation mode (Fig. 9).

The intensities of (1 1 1), (0 0 1) and (1 1 2) poles from the experimentally determined textures of the rails taken from service were matched with a shear strain level, such that they coincide with the hypothetical simulation results. Accordingly, the texture of BS low rail corresponds to a shear strain level of 1.00, and the BS high-rail texture intensities are equivalent to those of hypothetical simulation results at a shear strain of 1.10. Both of these values are well beyond the practical limit of 0.57 shear strain achieved in laboratory tests for this material. Similarly, the low- and high-rail textures of the PS correspond to shear strains of 0.95 and 1.10, which is again beyond the limit 0.61 attainable in the laboratory. The difference between the low and high rails of both materials is noticeable, indicating the evolution of texture with increasing amount of wear.

The change of level of anisotropy was also closely monitored at larger strains. To reflect this change, the Taylor factors were calculated for a polycrystalline aggregate under tensile loading following various levels of imposed simple shear deformation. At the shear strain levels for which the texture evolution was closely monitored (Fig. 9) the corresponding simulation textures were taken as the initial state of a polycrystalline aggregate subjected to uniaxial tension. The Taylor factors were calculated through Eq. (18) relating the yield strength levels obtained from VPSC simulations to the reference strength τ_0 that reflects the microscopic yield strength (Table 1). The results point out to an increasing Taylor factor (and therefore level of anisotropy) at larger strains (Figs. 10 and 11). Even at the initial state, prior to any shearing, for both BS and PS, the Taylor factors are different from that of a random polycrystalline aggregate, indicating the need for an anisotropic yield criterion for predicting the yield strength in shear. This need becomes more pronounced as the amount of previously imposed shear deformation on a material increases (Figs. 10 and 11). In order to verify the analysis conducted, the algorithm based on Bishop and Hill's work [30,31] was applied to the simulation textures at the shear strain levels of interest. The Taylor factors obtained were different to a second decimal only. The simulation results also agreed well with the stereographic maps of Taylor factors tabulated in Hosford's work [29] considering the change of texture with ongoing deformation.

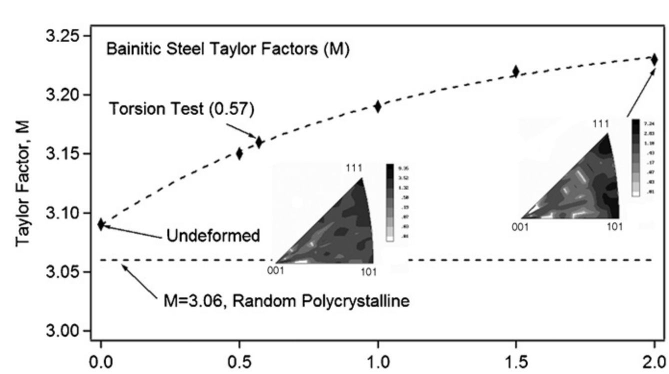

Fig. 10. Taylor factors (M) for BS obtained from simulations. Corresponding inverse pole figures for the undeformed state and predicted ones for 2.0 shear strain are shown. The degree of anisotropy increases with further deformation.

Please cite this article in press as: D. Canadinc, et al., Mater. Sci. Eng. A (2007), doi:10.1016/j.msea.2007.08.049

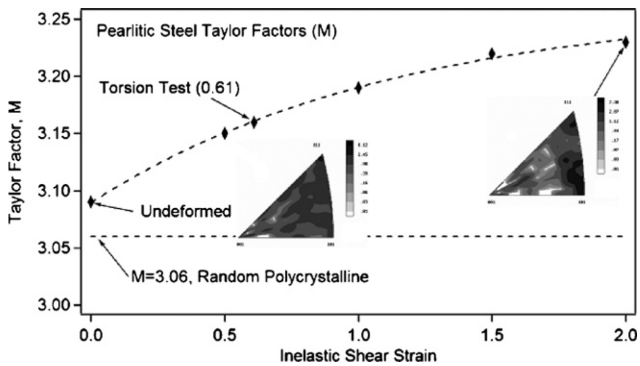

Fig. 11. Taylor factors (M) for PS obtained from simulations. Corresponding inverse pole figures for the undeformed state and predicted ones for 2.0 shear strain are shown.

7. Final remarks and discussion of results

7.1. Texture evolution

The work demonstrated that the experimentally measured textures of the worn rails could be matched to those of torsion simulations extending beyond the practical limits of the laboratory tests. This confirms that computer simulations provide insight where experimental data is difficult to obtain. The correspondence of the intensities of different poles at the same shear strain level is another indication of the success of the method used in the prediction of shear response utilizing the VPSC. The texture of the tested samples agreed very well with the simulations at the corresponding strains, supporting the idea of utilizing the texture as a means of determining the stress state of the rails taken from service.

It should be noted that the textures measured in the present study do not exactly represent those of the surface rail layer, but the layer(s) a few millimeters below. This explains the accumulated shear strain levels being well below the aforementioned values in the subsurface layers [33]. However, a detailed comparison focusing on this aspect is beyond the scope of the study presented herein.

7.2. Microstructure

Many virgin and deformed samples underwent transmission electron microscopy (TEM) with the purpose of monitoring the micro-mechanisms responsible for the observed deformation response. We do not show all the results here, as the microstructural observations have not hinted at any particular mechanism responsible for the stress–strain response exhibited. The different two-phase structures of the materials are evident, however no planar dislocation arrangements were visible, as expected. The lack of traces of any planar dislocation activities in the microstructure implies two possibilities: cross-slip or pencil glide.

When there is pencil glide, slip is possible on many systems in the ⟨1 1 1⟩ direction, making it hard to observe any dislocation arrangements or traces of planar arrangements. At this point, the present observations fall short of proving whether or not pencil glide is present in any of the materials under investigation. Therefore, only the primary slip on the (1 1 0)⟨1 1 1⟩ systems was considered active during the deformation of the bcc materials under consideration.

Even though not presented in this paper, the authors obtained results from similar simulations with simultaneous activation of the primary (1 1 0)⟨1 1 1⟩ and (1 1 2)⟨1 1 1⟩ slip systems, and all possible slip systems leading to pencil glide. The difference between these and the current observations were nothing more than a slight change in Voce hardening parameters and texture intensities of certain orientations. The general trend in the texture was preserved. Accordingly, for the sake of simplicity, the activation of only the primary slip in BS, PS and 1CRS was assumed. However, based on only this decision and the indifference between the simulation results, it is not correct to disregard the possibility of pencil glide, and the influence of pencil glide is left aside for future investigations.

The current model revealed useful information regarding the slip activity in the three materials of interest under shear loading (Fig. 12). Following an increase (up to 4.8) throughout a relatively short span of shear strain (0–0.2), the average number of active slip systems per grain decreases and saturates (at around 3.5) at larger shear strains (1.5–2.0). This observation agrees well with the expected texture evolution. As the shear deformation progresses, although no single crystallographic orientation becomes prominent, the texture evolves such that majority of the grains assume orientations in the vicinity of the (1 1 1)–(1 0 1) boundary (Fig. 8). The decreased number of preferred crystallographic orientations limits the average number of active slip systems at large strains, which brings about the decrease from 4.8 to 3.5 slip systems per grain. The saturation this number reaches, however, is expected, as the grains cannot assume a certain orientation over the others due to continuous rotation of the grains throughout the torsional deformation. Although individually some grains might assume a single or double slip orientation, most of the orientations assume multiple-slip orientations in the 3D space (Fig. 8).

7.3. Modeling of the stress–strain response

In the simulations, the Voce hardening rule was modified to account for the features of the pearlitic and bainitic microstructures, and then utilized to model the deformation response of

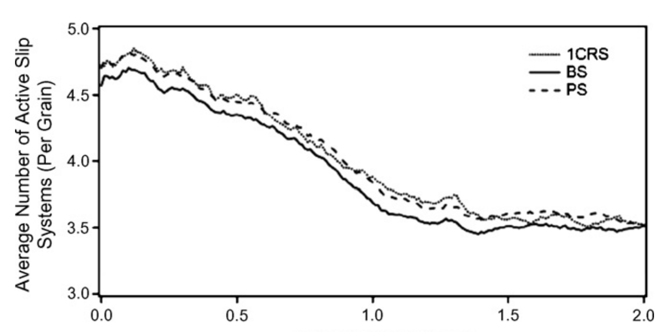

Fig. 12. Average number of active slip systems (per grain) with respect to inelastic shear strain for BS, PS, and 1CRS.

the materials. The plastic deformation was considered as independent of strain rate and temperature, and room temperature deformation response at slow strain rates was considered in this study. The strain rates and temperature experienced by rails under deformation can vary; however, the purpose of this study was to develop a methodology for predicting the deformation response and texture evolution of rail materials in shear, based on uniaxial tensile deformation response. Therefore, the focus was not placed on strain rate and temperature dependencies.

Two unique strain hardening formulations were successfully adopted to account for the important microstructural differences between the materials investigated. Specifically, a strain hardening formulation previously utilized to predict the deformation response of austenitic manganese steels that feature dense dislocation walls [14] was further modified to model the pearlite lamella–glide dislocation interaction in pearlitic steels (PS and 1CRS). As for the bainitic microstructure (BS), the corresponding deformation response was modeled by adopting a modified strain hardening scheme that successfully incorporates the precipitate hardening into the VPSC [20]. For both cases, however, substantial differences exist between the modified and the original Voce hardening formulations. For instance, in the case of dense dislocation walls (HDDWs), the HDDWs evolve in volume fraction due to continuous interaction with glide dislocations, such that the blocked dislocations add to the density of the HDDWs. In the current model, however, the pearlite lamellae do not evolve in volume fraction, and therefore, the corresponding volume fraction was fixed throughout the simulations. In the case of bainitic steel simulations, on the other hand, the difference was more substantial. In particular, the original model not only considers the contribution due to precipitate hardening, but also incorporates the twin-precipitate interactions that are prominent in nitrogen-alloyed Hadfield steels [20]. In the current approach, however, only the extra hardening contribution due to particle hardening was taken into consideration.

8. Conclusions

A crystal plasticity model was developed for the characterization of the body-centered cubic (bcc) railroad steels with pearlitic and bainitic microstructures, based on a combined experimental and simulation effort. Two unique strain hardening formulations were proposed that incorporate the length scales associated with pearlitic and bainitic microstructures into a visco-plastic self-consistent (VPSC) algorithm. Simple uniaxial tension test data and crystallographic texture were employed to establish the parameters defining the deformation response of the materials. The simulation of the simple shear (torsion) and compressive deformation modes were predicted favorably. By relating the macroscopic tensile deformation response to the deformation at the grain level based on slip systems, the hardening parameters were established that led to the successful prediction of the yield strength in shear and its evolution. Extension of our simulations to strains beyond those observed in the laboratory but encountered in service predicted the change in texture intensities due to plastic deformation. Texture at hypothetically high strains was used as a means of determining the stress state of the rails taken from service. Finally, the texture results confirm the need for developing numerical methods, such as the one presented herein, in order to acquire information that is not available from laboratory experiments. Furthermore, the incorporation of length scales associated with lamellar spacing and particle hardening due to carbides in the bainite structure into crystal plasticity models, as successfully demonstrated in the current work, will assist new material development efforts.

Acknowledgements

This work was ~~supported~~ by the Association of American Railroads (AAR)/Transportation Technology Center Inc. (TTCI) and the Federal Railway Administration (FRA). The German part of the study was supported by Deutsche Forschungsgemeinschaft (DFG) within the Transregional Collaborative Research Center TRR30. Mr. Joe Kristan and Mr. David Davis of AAR/TTCI are thanked for their support and assistance. The authors are grateful to Dr. Carlos Tomé for kindly offering the Code VPSC Version 5.0 to be used in the modeling effort presented in this paper.

References

[1] K. Sawley, J. Kristan, Fatigue Fract. Eng. Mater. Struct. 26 (2003) 1019.
[2] K. Sawley, R. Jimenez, AAR Research Report No. R-941, 2000.
[3] K.M. Lee, A.A. Polycarpou, Wear 259 (2005) 391.
[4] Courtesy of AAR/TTCI.
[5] K.S. Havner, Finite Plastic Deformation of Crystalline Solids, Cambridge University Press, New York, 1992.
[6] J. Weertman, J.R. Weertman, Elementary Dislocation Theory, Oxford University Press, New York, 1992.
[7] G.I. Taylor, C.F. Elam, Proc. Roy. Soc. Lond. A 112 (1926) 337.
[8] G.I. Taylor, Proc. Roy. Soc. Lond. A 118 (1928) 1.
[9] C.F. Elam, Proc. Roy. Soc. Lond. A 153 (1936) 273.
[10] U.F. Kocks, C.N. Tomé, H.R. Wenk, Texture and Anisotropy, Cambridge University Press, New York, 1998.
[11] A.D. Rollett, U.F. Kocks, ICOTOM 8 (1987) 375.
[12] P. Gilormini, B. Bacroix, J.J. Jonas, ICOTOM 8 (1987) 381.
[13] P. Van Houtte, ICOTOM 5 (1978) 347.
[14] D. Canadinc, H. Sehitoglu, H.J. Maier, Y.I. Chumlyakov, Acta Mater. 53 (2005) 1831.
[15] R.A. Lebensohn, C.N. Tomé, Acta Metall. Mater. 41 (1993) 2611.
[16] R.A. Lebensohn, C.N. Tomé, Manual for Code Visco-Plastic Self-Consistent, 2002.
[17] P.A. Turner, C.N. Tomé, N. Christodoulou, C.H. Woo, Philos. Mag. A 79 (1999) 2505.
[18] D. Canadinc, H. Sehitoglu, H.J. Maier, D. Niklasch, Y.I. Chumlyakov, Int. J. Solids Struct. 44 (2007) 34.
[19] D. Canadinc, H. Sehitoglu, H.J. Maier, Mater. Sci. Eng. A 454–455 (2007) 662.
[20] D. Canadinc, I. Karaman, H. Sehitoglu, Y.I. Chumlyakov, H.J. Maier, Metall. Mater. Trans. A 34 (2003) 1821.
[21] P. Bate, W.T. Roberts, D.V. Wilson, Acta Metall. Mater. 29 (1981) 1797.
[22] L.M. Brown, G.R. Woolhous, Philos. Mag. 21 (1970) 329.
[23] L.M. Brown, W.M. Stobbs, Philos. Mag. 23 (1971) 1185.
[24] L.M. Brown, W.M. Stobbs, Philos. Mag. 23 (1971) 1201.
[25] F. Barlat, J. Liu, Mater. Sci. Eng. A 257 (1998) 47.
[26] T. Mura, Micromechanics of Defects in Solids, Kluwer Academic Publication, 1993.

Please cite this article in press as: D. Canadinc, et al., Mater. Sci. Eng. A (2007), doi:10.1016/j.msea.2007.08.049

[27] E. Nembach, Particle Strengthening of Metals and Alloys, John Wiley & Sons Inc., 1997.
[28] W.A. Spitzig, Acta Metall. 29 (1981) 1359.
[29] W.F. Hosford, The Mechanics of Crystals and Textured Polycrystals, Oxford University Press, New York, 1993.
[30] J.F.W. Bishop, R. Hill, Philos. Mag. 42 (1951) 414.
[31] D. Canadinc, H. Sehitoglu, Unpublished work.
[32] J. Lubliner, Plasticity Theory, Macmillan Publishing Company, USA, 1990.
[33] F.J. Franklin, I. Widiyarta, A. Kapoor, Wear ~~2110~~ (251) 949. **Q2**

Please cite this article in press as: D. Canadinc, et al., Mater. Sci. Eng. A (2007), doi:10.1016/j.msea.2007.08.049